

M.N.A. Beurskens, T.H. Osborne, L.D. Horton, L. Frassinetti, R. Groebner,
A. Leonard, P. Lomas, I. Nunes, S. Saarelma, P.B. Snyder, I. Balboa, B. Bray,
K. Crombé, J. Flanagan, C. Giroud, E. Giovannozzi, M. Kempenaars, N. Kohen,
A. Loarte, J. Lönnroth, E. de la Luna, G. Maddison, C. Maggi, D. McDonald,
G. McKee, R. Pasqualotto, G. Saibene, R. Sartori, E. Solano, W. Suttrop,
E. Wolfrum, M. Walsh, Z. Yan, L. Zabeo, D. Zarzoso
and JET EFDA contributors

Pedestal Identity Studies in JET, DIII-D and implications for ITER

“This document is intended for publication in the open literature. It is made available on the understanding that it may not be further circulated and extracts or references may not be published prior to publication of the original when applicable, or without the consent of the Publications Officer, EFDA, Culham Science Centre, Abingdon, Oxon, OX14 3DB, UK.”

“Enquiries about Copyright and reproduction should be addressed to the Publications Officer, EFDA, Culham Science Centre, Abingdon, Oxon, OX14 3DB, UK.”

Pedestal Identity Studies in JET, DIII-D and implications for ITER

M.N.A. Beurskens¹, T.H. Osborne², L.D. Horton, L. Frassinetti³, R. Groebner²,
A. Leonard², P. Lomas¹, I. Nunes⁴, S. Saarelma¹, P.B. Snyder², I. Balboa¹, B. Bray²,
K. Crombé⁵, J. Flanagan¹, C. Giroud¹, E. Giovannozzi⁶, M. Kempenaars¹, N. Kohen⁷,
A. Loarte⁸, J. Lönnroth⁹, E. de la Luna¹⁰, G. Maddison¹, C. Maggi¹¹, D. McDonald¹,
G. McKee¹², R. Pasqualotto¹³, G. Saibene¹⁴, R. Sartori¹⁴, E. Solano¹⁰, W. Suttrop¹¹,
E. Wolfrum¹¹, M. Walsh¹, Z. Yan¹², L. Zabeo¹, D. Zarzoso¹⁵
and JET EFDA contributors*

JET-EFDA, Culham Science Centre, OX14 3DB, Abingdon, UK

¹EURATOM-UKAEA Fusion Association, Culham Science Centre, OX14 3DB, Abingdon, OXON, UK

²General Atomics, PO Box 85608, San Diego, CA 92186-5608, USA

³Association EURATOM-VR, Alfvén Laboratory, School of Electrical Engineering, KTH, Stockholm, Sweden

⁴Centro de Fusão Nuclear, Associação EURATOM-IST, Lisboa, Portugal

⁵Department of Applied Physics, Ghent University, Rozier 44, 9000 Gent, Belgium

⁶Associazione EURATOM-ENEA sulla Fusione, Consorzio RFX Padova, Italy

⁷University of Marseille, France

⁸ITER Organization, CS 90 046, F-13067 Saint Paul lez Durance Cedex, France

⁹Association EURATOM-Tekes, Helsinki University of Technology, Finland

¹⁰Asociación EURATOM-CIEMAT para Fusión, Madrid, Spain

¹¹Association EURATOM-Max-Planck-Institut für Plasmaphysik, D-85748 Garching, Germany,

¹²University of Wisconsin, Madison WI, USA

¹³Associazione EURATOM-ENEA sulla Fusione, C.R. Frascati, Frascati, Italy

¹⁴FUSION FOR ENERGY Joint Undertaking, 08019 Barcelona, Spain.

¹⁵Ecole Polytechnique, F-91128, Palaiseau cedex, France

* See annex of F. Romanelli et al, "Overview of JET Results",
(Proc. 22nd IAEA Fusion Energy Conference, Geneva, Switzerland (2008)).

Preprint of Paper to be submitted for publication in Proceedings of the
36th EPS Conference on Plasma Physics, Sofia, Bulgaria.
(29th June 2009 - 3rd July 2009)

ABSTRACT.

The dependence of the H-mode edge transport barrier width on normalized ion gyro radius ($\rho^* = \rho/a$) in discharges with Type I ELMs was examined in experiments combining data for the JET and DIII-D tokamaks. The plasma configuration as well as the local normalised pressure (β), collisionality (ν^*), Mach number, and the ratio of ion and electron temperature at the pedestal top were kept constant, while ρ^* was varied by a factor of four. The width of the steep gradient region of the electron temperature (T_e) and density (n_e) pedestals normalized to machine size showed no or only a weak trend with ρ^* . A $\rho^{1/2}$ or ρ^1 dependence of the pedestal width, given by some theoretical predictions, is not supported by the current experiments. This is encouraging for the pedestal scaling towards ITER as it operates at lower ρ^* than existing devices. Some differences in pedestal structure and ELM behaviour were however found between the devices; in the DIII-D discharges, the n_e and T_e pedestal were aligned at high ρ^* but the n_e pedestal shifted outwards in radius relative to T_e as ρ^* decreases, while on JET the profiles remained aligned while ρ^* was scanned by a factor of two. The energy loss at an ELM normalized to the pedestal energy increased from 10% to 40% as ρ^* increased by a factor of 2 in the DIII-D discharges but no such variation was observed in case of JET. The measured pedestal pressures and widths were found to be consistent with the predictions from modelling based on peeling ballooning stability theory.

1. INTRODUCTION

The H-mode pedestal, the region of strongly reduced transport just inside the limiting flux surface, has important effects on both the entire confined core region and the scrape-off layer plasma in a tokamak. A strong coupling of the pedestal and core confinement has been observed in many devices [32]. Therefore, the ITER fusion performance is predicted [10] to increase strongly with the achievable pedestal pressure. In order to meet the design goals of ITER [29] a pedestal temperature of 4keV is required (depending on the degree of core profiles stiffness predicted by the particular turbulent transport model [10]), at the density needed to achieve the required fusion power output. As the pedestal pressure gradient is limited by MHD stability through either ideal ballooning or combined peeling-ballooning stability [3, 4, 44, 39, 9, 33], the pedestal width plays an important role in determining pedestal pressure, p_{ped} . From MHD stability analysis one can infer then that ITER would require a pedestal width of 2.5% of the minor radius to reach the required $T_{ped} = 4keV$ [25, 40].

At plasma-facing surfaces, particularly the divertor targets, melting and ablation limits place severe constraints on the maximum plasma energy loss per ELM in ITER. A maximum tolerable ELM energy loss limit of $\Delta W_{ELM} = 1MJ$, which corresponds to $\sim 1\%$ of the pedestal stored energy ($W_{ped} = 3/2 * P_{PED} * \text{plasma volume}$) has recently been set [45]. In a multi device comparison it was found that the relative ELM size scales inversely with pedestal collisionality ($\nu^* \propto n_{ped}/T_{ped}^2$) [15, 2]. Given the required high T_{ped} , this scaling predicts an unacceptably large ELM size, $\Delta W_{ELM}/W_{ped} > 15\%$, for ITER, however the physics of the ELM energy loss remains uncertain and dependencies other than ν^* cannot be ruled out. It has been suggested in [39] that the pedestal width also plays a role in determining the ELM size. A wider steep gradient region results in lower

toroidal mode number instabilities with a larger radial extent. Although these linear MHD results are unlikely to accurately describe the nonlinear ELM dynamics, the more radially extended modes might affect a larger region of the plasma, and there is experimental correlation between the mode width and the ELM size on DIII-D and JT-60U [12, 27].

A number of theoretical arguments have been made as to what might set the extent of the ExB velocity shear turbulence suppression zone in the H-mode edge [8, 23, 25]. Width scalings are typically derived either based on the extent of the region where there is strong drive for the velocity shear, or on the point where the turbulence drive overcomes the velocity shear. Examples of the former include: 1) the velocity shear being driven by $J \times B$ forces associated with ion orbit loss leading to a width scaling like the ion banana width $w \propto \rho_{pi}$ ($\rho_{pi} \propto \sqrt{T_i/B_p}$), 2) the velocity shear being driven by the particle flux associated with the edge neutral particle source suggesting a width scaling like the neutral penetration depth, $w \propto 1/n_{ped}$. For drift waves the point where the turbulence overcomes the velocity shear is expected to be the point where the linear growth rate exceeds the ExB velocity shearing rate. This leads to a width dependence on the ion gyroradius ($\rho_{tor} \propto \sqrt{T_i/B_T}$) ranging from $w \propto \rho_{tor}^{1/2}$ to $w \propto \rho_{tor}$ depending on the assumed linear growth rate scaling. A new theoretical model, EPED1, [42] proposes that, after the drift wave turbulence is suppressed by ExB velocity, the onset of short wavelength kinetic ballooning mode turbulence constrains the pedestal to a critical normalized pressure gradient, α_C . Since $\alpha \propto \beta_p/w_\psi$, where $\beta_p \propto p_{ped}/\langle B_p^2 \rangle$ is the pedestal poloidal β , this gives a relation between the pedestal width and height, approximately $w_\psi \propto \beta_p^{1/2}$ once magnetic shear dependence is accounted for. This constraint is approximately consistent with earlier empirical scaling of the width as $w \propto \beta_p^{0.4}$ [24]. A further relation between the width and height is provided by the peeling-ballooning mode instability onset condition for the ELM. These two constraints are resolved to an operating point for the width and height in EPED1. EPED1 has been used successfully to predict pedestal conditions in DIII-D and other tokamaks [42, 41].

A positive dependence of pedestal width on the ion gyro radius is a concern for ITER as it will operate at significantly smaller normalised gyro radius ρ^* than current devices [13]. Experiments carried out on a single device by either a gas scan, varying the magnetic field, or changing ion isotope mass observed no or only a weak dependence of the pedestal width on gyro radius [24, 34, 25, 11, 43]. However in earlier experiments in JT-60U [7] and later with new JT-60U data in the ITPA pedestal database in [25], a strong dependence on ρ_{pi} was found. These earlier experiments however were either limited by the range of ρ^* that could be achieved on a single device, or by a mixing of the ρ^* variation with other effects. Therefore a high priority is to conduct multi machine ρ^* similarity experiments where only ρ^* is varied over a wide range.

Experiments in which all the dimensionless quantities were matched at the top of the pedestal on two different tokamaks indicate that the electron temperature pedestal width scales with machine size, $w_{Te}^* \approx 3\%$ [20, 26, 5, 13]. However there are differences in the behaviour of the density pedestal width, which plays an equally important role in setting the pedestal pressure height and gradient. In a comparison of DIII-D and Alcator C-mod $w_{ne}^* \approx 3\%$ [20], however between JET

and DIII-D [26, 5] and JET and Alcator C-mod [17] $w_{ne}^* \propto 1/n_{ped} \propto$ neutral mean free path [6, 18], while on AUG the pedestal in Type I ELMy H-modes remains unvaried for a wide range of pedestal densities [21, 22]. In experiments on DIII-D in which pedestal ρ^* was varied by a factor of 1.6 keeping other dimensionless parameters fixed [5], no variation of the temperature pedestal width was found and $w^*_{Te} \sim 3\%$. The density pedestal width however increased with ρ^* and showed a $w_{ne} \sim 1/n_{ped}$ dependence. In addition in the DIII-D experiment a large increase of $\Delta W_{ELM}/W_{ped}$ from 10% to 40% was found when ρ^* was increased (at fixed v^*). Following [40] it was confirmed that the larger ELM size was correlated with the wider density pedestal width at low n_{ped} . In the experiments described in this paper, new high resolution diagnostic capability on JET in combination with DIII-D results have facilitated significantly extending the range of \mathfrak{S}^* to a factor of 4.

In section 2 of this paper the experimental conditions are described. The ELM characteristics and the pedestal scaling analysis is discussed in respectively sections 3 and 4. Two sensitivity studies on JET are reported in section 5, in which 1) the pedestal collisionality and 2) the magnetic field ripple was varied. Then the experimental results are compared to modelling using EPED1 and ELITE in section 6, followed by conclusion in section 7.

2. EXPERIMENTAL CONDITIONS

JET and DIII-D are similarly shaped devices with ITER-like geometries. Both devices have similar poloidal divertor configurations with JET being a factor of 1.8 larger in linear dimension than DIII-D: JET [$R = 2.95\text{m}$, $a = 0.95\text{m}$], DIII-D: [$R = 1.67\text{m}$, $a = 0.54\text{m}$], with (R) the major and (a) the minor radius. For the experiments reported here the plasma shape was matched as closely as possible with upper and lower triangularities of $\delta_u \sim 0.2$ and $\delta_l \sim 0.4$ and elongation of $\kappa \sim 1.7$. Figure 1a shows the plasma shape match for the experiments. The lower outer squareness and lower triangularity were not perfectly matched because of a difference in the divertor coil geometry between JET and DIII-D.

Maintaining fixed normalised pressure $\beta_{ped} = p_{ped}/(B_T^2/2\mu_0)$, collisionality $v^* = q \times R^{5/2} \times a^{-3/2} \times (\lambda_{e,e})^{-1}$ (where $\lambda_{e,e} \approx 2.245 \times 10^{18} T_e^2 \text{ (eV)} / n_e \text{ (m}^{-3}\text{)}$, e.g. [15]) and safety factor q at the top of the pedestal requires that (at fixed aspect ratio) the density, temperature, and plasma current scale with minor radius and toroidal field as $n_{ped} \propto a^{-1/3} B_T^{4/3}$, $T_{ped} \propto a^{1/3} B_T^{2/3}$, and $I_p \propto B_T$, giving a ρ^* variation as $\rho^* \propto a^{-5/6} B_T^{-2/3}$. This means that at the dimensionless identity point where ρ^* is matched as well, $n_{ped, DIII-D} \approx 3 \times n_{ped, JET}$, $T_{ped, DIII-D} \approx 1.3 \times T_{ped, JET}$, $B_{T, DIII-D} \approx 2 \times B_{T, JET}$, and $I_{p, DIII-D} \approx 1.1 \times I_{p, JET}$. The parameters chosen for the identity experiment are $I_p = 1.0\text{MA}$, $B_T = 1.1\text{T}$ for JET and $I_p = 1.1\text{MA}$ and $B_T = 2.1\text{T}$ for DIII-D. The ρ^* scan is achieved by varying the magnetic field on JET in three steps as $B_T = 1.1\text{T}$, 1.8T and 2.7T and on DIII-D as $B_T = 1\text{T}$, 1.4T and 2.1T . The neutral beam input power was varied on JET from $P_{NBI} = 4.5$ to 15MW and on DIII-D from 1.5 to 9MW . At the higher field a small amount of ion cyclotron heating of $P_{ICRH} = 1\text{MW}$ was applied on JET to avoid density peaking.

The main pedestal profile diagnostics used on JET is the new High Resolution Thomson Scattering system (HRTS, with a 20Hz, 5J, 1064nm, Nd:YAG laser) [30]. It measures profiles of T_e and n_e on the outboard side magnetic mid plane, $R=2.9\text{-}3.9\text{m}$, with an accuracy in T_e of better than 10% at

$n_e = 10^{19} \text{ m}^{-3}$. It has 61 spatial points with a 1.5cm interpoint spacing and a 2cm spatial resolution. As a comparison the typical pedestal width for JET is 3cm. To increase the density of measurement points in the pedestal, the plasma is moved radially by 1.5cm on a 5 second duty cycle and data is accumulated from the last 30% of the ELM cycle for many ELMs [1]. A similar technique is used to measure the electron profiles on DIII-D [5], where the spatial resolution is roughly 0.5cm on the outboard midplane compared to a typical pedestal width of 1.5–2cm. Since the pedestal widths are near the resolution of the HRTS systems, a forward deconvolution procedure is applied in fitting the data. A modified hyperbolic tangent (mtanh) [6] is taken for the functional form of the data without the instrumental effects. For the n_e profile, which depends only on the magnitude of the scattered laser light, the mtanh function is convolved with the HRTS instrument profile kernel before applying the least square fit. The instrumental effects on the T_e profile are more complex, involving the response of the polychromators to mixtures of temperature spectra [e.g. Scannell-2006]. In this paper we approximate these effects by multiplying the instrumental kernel by the density profile before convolving with the mtanh function. These corrections for the instrumental effects reduce the n_e width by about 20% for JET and about 5% for DIII-D, while the temperature width on JET is reduced by 30-40% and on DIII-D by 15-20%. The ion temperature profiles in the case of JET are typically measured with a 4cm spatial resolution. On DIII-D the ion profile measurements have a spatial resolution similar to the electrons, 0.4cm on the outboard midplane. No corrections are made to the ion profiles for instrumental effects.

3. ELM BEHAVIOUR AND H-MODE CHARACTERISTICS.

In this section the ELM behaviour of the pulses in the ρ^* pedestal similarity scan are described. Figure 1b shows the divertor D_α signal for all the pulses. The JET low ρ^* point (Pulse No: 75977) features a low ELM frequency with occasional compound phases following Type I events. The intermediate ρ^* discharges on JET (Pulse No's: 73927 and 73916) all feature simple type I ELMs, whereas the next two DIII-D discharges feature mixed Type I/Type II ELMs (Pulse No's: 136051 and 136062). At the highest ρ^* point on DIII-D (Pulse No: 136069) the ELM frequency is slightly reduced and the type II ELMs are not present. Figure 1c shows the ELM energy losses normalized to the pedestal energy, $\Delta W_{\text{ELM}}/W_{\text{ped}}$. They range from 10-20% for the JET discharges to ~40% for the highest ρ^* point at DIII-D. For this analysis the compound and type II ELM phases are excluded and the energy losses are calculated for the Type I ELMs only. A strong positive trend with ρ^* is observed for the DIII-D plasmas. A comparison with the multi device ELM loss database [15], Figure 1d, shows that the new JET data are consistent with what would be expected given the pedestal collisionality [15], while the high ρ^* DIII-D data show a much larger than expected energy loss. For all pulses in this study the input power is well above the L-H power threshold as given in [19] and $P_{\text{in}} > 1.5P_{\text{L-H}}$. Therefore the proximity to the threshold cannot explain the large variation in ELM size. The high ρ^* DIII-D data also deviates strongly from the old DIII-D data in Figure 1d which have lower pedestal ρ^* .

MHD analysis using measured profiles and the ELITE linear stability code [39], shows that all

discharges are near the peeling-ballooning instability threshold with similar mode structures. Although the mode structure is slightly broader in the DIII-D high ρ^* cases, the difference is small compared to the observed large increase in ELM size.

4. PEDESTAL STRUCTURE ANALYSIS

The pedestal profile data in the ρ^* scan as a function of the distance of the data points from the separatrix, $rlcfs$, normalized to minor radius are shown in Figure 2. This figure indicates the accuracy with which the other dimensionless parameters were held fixed at the top of the pedestal as ρ^* was varied as well as giving an idea of experimental error for these quantities. In addition, because of uncertainties in the position of the separatrix in the equilibrium reconstruction, the lower inflection points of the temperature pedestals have been aligned with the separatrix. This alignment of the temperature profiles is justified by the requirement that the separatrix temperature be $\sim 100\text{eV}$ to satisfy conditions at the divertor plate, and by detailed divertor modelling of DIII-D discharges [31]. At $\rho^*_{\text{ped}} \approx 0.004$ all dimensionless quantities were well matched between JET and DIII-D (Figure 2 (a, b, d, e)) where $n_{\text{ped, DIII-D}} \approx 3 \times n_{\text{ped, JET}}$ and $T_{\text{ped, DIII-D}} \approx 1.3 \times T_{\text{ped, JET}}$. At the pedestal top, ρ^* was varied by a factor of four from ~ 0.002 to ~ 0.008 (figure 2g). Through the ρ^* variation, β was well matched, while v_e^* , which is highly sensitive to T_e , n_e and q , was matched only to within a factor of two. The q profile disagreement was caused by the shape mismatch resulting in about a 10% difference at the pedestal top. In addition the effective atomic charge number Z_{eff} (not shown) and T_e/T_i was well matched at lower ρ^* and at the identity point ($Z_{\text{eff}} \approx 1.5$, $T_e/T_i \approx 1$) but deviated for the higher ρ^* points ($\rho^*_{\text{ped}} \approx 0.006$: $Z_{\text{eff}} \approx 2$, $T_e/T_i \approx 0.9$, $\rho^*_{\text{ped}} \approx 0.008$: $Z_{\text{eff}} \approx 2.5$, $T_e/T_i \approx 0.7$).

The shapes of the normalized electron temperature profiles in the pedestal closely match at the dimensionless parameter match point (Figure 2e) and throughout the ρ^* scan (Figure 2f); however the relative positions of the T_e and n_e profiles differ in the two devices (Figures 2b,e). At JET the T_e and n_e pedestal align, whereas on DIII-D the density pedestal is about half a pedestal width further out in radius than the temperature pedestal. This position offset between the n_e and T_e profiles is reduced when ρ^* is increased in the DIII-D scan, as can be seen in Figure 2c. In the JET scan the relative offset between the n_e and T_e profiles remains near zero when ρ^* is decreased by a factor of two. At the highest value of ρ^* in DIII-D, the density profile aligns with the JET profiles.

The T_e and n_e pedestal width and density pedestal offset variation with ρ^* are obtained by applying the $m \tanh$ fitting procedure with deconvolution to the profiles (Figure 3). Both the T_e and n_e widths remain fixed at 2.5 to 3% of the minor radius through the factor of 4 variation in ρ^* . The error bars in figure 3 are determined from the scatter of the data about the fit lines weighted with the statistical instrumental uncertainties. Special treatments are applied to the error analysis of the data near the pedestal foot. Because data is accumulated from many inter-ELM periods by mapping to equilibrium reconstructions at the individual profile times, variations in the alignment between the data and equilibrium cause an effective smearing of the composite profile in radius. Since the present $m \tanh$ fitting procedure includes errors in the measured value but not the position, this smearing can skew the profiles in the foot region where the statistical value error is typically very small. Two

methods were used to adjust for this effect. In method 1 a minimum value error of 30% of the median error is applied to all the data; in method 2, data with value errors > 100% (most of the data in the T_e foot) are dropped in the fit. Method 1 gives $w_{T_e}/a \propto (\rho^*)^{-0.15 \pm 0.10}$ and $w_{n_e}/a \propto (\rho^*)^{0.13 \pm 0.08}$ while method 2 gives $w_{T_e}/a \propto (\rho^*)^{0.01 \pm 0.13}$ and $w_{n_e}/a \propto (\rho^*)^{0.15 \pm 0.09}$. The χ^2 probability (probability that the χ^2 with this exponent could be due to statistical error) as a function of the ρ^* exponent for the two methods for accounting for the R smearing applied to fitting the w_{T_e}/a data is show in figure 4, as well as the F test probability between the minimum χ^{2v} value and other exponents. Clearly a $w^* \propto (\rho^*)^{1/2}$ or $w^* \propto (\rho^*)^1$ dependence as is predicated by some theories (see section 1) is not supported by the data. The implications of a possible weak ρ^* dependence is discussed in section 5.

To study the effect of neutral penetration depth, the definition of the density pedestal width as described in [18] and [6] is used. Figure 3c shows the density pedestal width inside the separatrix $w_{n_e, \text{separatrix}} = (R^{\text{sep}} - R^{\text{ped}})$ where the separatrix position is defined as the lower T_e inflection point. In JET this definition leads to a similar width as in Figure 3b since the T_e and n_e profiles are aligned throughout the JET scan. However, the relative position of the DIII-D T_e and n_e profiles varies in the scan and the density width up to the separatrix increases with ρ^* . The neutral penetration model [6] predicts $w_{n_e, \text{separatrix}} \propto 1/n_{\text{ped}} E^*$ where E^* is the poloidally averaged flux expansion weighted with the magnitude of the neutral particle source. Substituting the n_{ped} scaling required in the ρ^* scan ($n_{\text{ped}} \propto a^{-1/3} B_T^{4/3}$), the neutral penetration model gives $w_{n_e, \text{separatrix}}^* \propto a(\rho^*)^2/E^*$. While the DIII-D data is in rough agreement with $w_{n_e, \text{separatrix}} \propto (\rho^*)^2$, $w_{n_e, \text{separatrix}}$ does not vary with ρ^* in JET and is above the expected value assuming the same poloidal distribution of neutral source in the two tokamaks. On DIII-D the particle source is concentrated in the divertor region where $E^* \sim 7-9$. A much lower value of E^* is required for JET to make the measurements match the neutral penetration model; i.e. if the JET neutral source were distributed more evenly poloidally and the ne pedestal could not expand beyond the transport barrier represented by the T_e pedestal, this might account for $w_{n_e, \text{separatrix}}$ in JET within the neutral source picture. However, detailed divertor modelling would be required to study this difference, which is beyond the scope of this paper.

5. SENSITIVITY STUDIES ON PEDESTAL WIDTH: EFFECT OF COLLISIONALITY AND RIPPLE

Since some variation in collisionality occurred in the ρ^* scan, a study of the sensitivity of the pedestal width to $v^* \propto n/T^2$ was also carried out. The electron collisionality was varied by gas fuelling from $v_{e, \text{ped}}^* \approx 0.15$ to $v_{e, \text{ped}}^* \approx 0.45$ about the JET dimensionless identity point ($\delta_{\text{av}} = 0.28, I_p = 1\text{MA}$ and $B_T = 1.1\text{T}, P_{\text{NBI}} = 4.5\text{MW}$). Figure 5 shows the comparison of the $n_e, T_e, v_{e, \text{ped}}^*$ profiles in this scan. It is clear that despite the wide range of $v_{e, \text{ped}}^*$ covered the pedestal width is not affected.

Since the toroidal field ripple was found to affect the pedestal confinement and therefore also possibly the pedestal structure [36, 37], and the nominal ripple values differ between JET (0.08%) and DIII-D (0.3%), a sensitivity study was also conducted on the effect of ripple on the ρ^* scan results. The ripple on JET was varied from 0.08% to 1% in steps of $\sim 0.25\%$ at constant absorbed neutral beam power of $P_{\text{NBI}} = 4.5\text{MW}$. The pedestal n_e and T_e profiles as well as T_e/T_i were unchanged

as the ripple was varied; only the toroidal rotation profile was affected (Figure 6). This result is in contrast with observations at higher current and field on JET [36, 37], where a clear degradation of edge confinement was observed over a similar ripple range. However it is worth noting that the current experiment shows no density pump-out as a result of ripple as was found in [37]. At identity point a direct comparison of the pedestal profiles in JET and DIII-D is allowed as under these conditions the confinement is not affected in the ripple scan.

6. MODELLING OF THE PEDESTAL HEIGHT AND WIDTH; IMPLICATIONS FOR ITER.

Predictions by the EPED1 model, which is described in section 1, are in good agreement with the pedestal pressures and widths obtained in the ρ^* scan (Figure 7) and are within the measurement and model uncertainties. The width constraint in EPED1 is derived from kinetic ballooning mode theory and is given by $w_\Psi = C(\beta_{p,ped})^{1/2}$ where w_Ψ the pedestal width in normalised poloidal flux and C a constant. The pedestal height is then derived from peelingballooning mode stability calculations using the ELITE code [39]. Moreover the proportionality constant C between w_Ψ and $(\beta_{p,ped})^{1/2}$ is obtained from an empirical scaling using a large database of DIII-D discharges and is found to be $w_\Psi = (0.077 \pm 0.016)(\beta_{p,ped})^{1/2}$. The implication of the uncertainty in C for the EPED1 predictions is show by the dotted lines in figure 7. Fitting all the ρ^* scan data set w/w_{EPED1} to a constant gives $w/w_{EPED1} = 1.04 \pm 0.03$.

EPED1 has been employed to predict the ITER pedestal [42] for a variant of ITER scenario 2 ($I_p = 15\text{MA}$, $\beta_N = 1.8$, $n_{ped} = 7 \times 10^{19} \text{m}^{-3}$, [29]), giving $w \gg \sim 0.04$, which corresponds to $w/a \sim 2.3\%$, and $\beta_{N,ped} \sim 0.6-0.7$, corresponding to a temperature of $\sim 4.6\text{keV}$ at $n_{ped} = 7 \times 10^{19} \text{m}^{-3}$. However, EPED1 does not explicitly include a ρ^* dependence of the pedestal width w_Ψ . Given the uncertainties in the ρ^* dependence of the width discussed in section 3, a sensitivity study was performed based on the actual profile measurements. A discharge at ITER minor radius and $B_T = 5.3\text{T}$ with the same shape, q , v_e^* , and β_{ped} as the dimensionless parameter match discharges in the ρ^* scan would have $I_p = 10.5\text{MA}$, $T_{ped} = 2.2\text{keV}$, and $n_{ped} = 8.4 \times 10^{19} \text{m}^{-3}$. As the projected pedestal density is now above the Greenwald density limit it is reduced to 90% of the Greenwald fraction, $n_{ped} = 7.4 \times 10^{19} \text{m}^{-3}$, somewhat sacrificing the v^* match. In order to preserve β , the pedestal T_e becomes 2.5keV . At this temperature (assuming $T_i = T_e$) and field, ρ^* at the pedestal top in ITER will be ~ 0.001 .

Figure 8 shows the result of a stability analysis using the ELITE code (first use on JET with HRTS data in [1, 33]) and the T_e and n_e profiles from the JET low ρ^* point (Pulse No: 75977) scaled to ITER. In this modelling n_{ped} was kept fixed at $7.4 = 7.4 \times 10^{19} \text{m}^{-3}$ and T_{ped} was increased until the stability limit was reached. This results in a predicted $T_{ped} = 2.5\text{keV}$ for ITER at the same w/a as the JET discharge, which is in agreement with the dimensionless scaling. Next the pedestal width was varied and the T_{ped} again calculated at fixed pedestal density. Figure 8 shows that if both the temperature and density width are varied from $w^* = 0.02$ to 0.036 the pedestal height varies by more than a factor of two from 1.7keV to 3.5keV . If only the temperature width is varied over the same range then the pedestal temperature varies from 2.0 to 2.8keV . This analysis shows that small variations in the pedestal

width can have strong implications on the predicted pedestal height, and that it is important to know both the T_e and n_e width scaling accurately. The results in section 4 show that the T_e and n_e pedestal widths show no strong ρ^* dependence, however even a weak dependence can have a significant impact on the pedestal performance. A dependence of only $w^* \propto (\rho^*)^{0.175}$ would reduce the predicted width for ITER from $w^* = 0.03$ to 0.02 which cannot be excluded by the data in Figure 3.

Finally a sensitivity study was conducted in order to study the effect of the relative profile shift found in DIII-D. The density profile of JET Pulse No: 75977 has been shifted outward by $r/a = 0.01$ and the T_e and n_e profiles have otherwise been left untouched. Using these profiles and the ELITE stability analysis gives a prediction of the pedestal temperature 10% below the value obtained with the unperturbed profile position (Figure 8).

CONCLUSIONS

The experiment presented in this paper show that the pedestal width of both T_e and n_e show no or only a weak dependence on ρ^* . A linear or square root scaling with ρ^* of the pedestal width, as suggested by some theories, is not supported by the experiment. However it has been demonstrated that a weak trend as $w^* \propto (\rho^*)^x$ with $x = 0.1-0.2$ cannot be excluded by the experimental results. Nevertheless the exclusion of a strong ρ^* dependence of the pedestal width with a high degree of certainty is positive news for extrapolation to ITER.

The relative position shift of the density and temperature pedestal as observed on DIII-D has been studied; a simulation shows that the maximum obtainable pedestal temperature is reduced by 10% when the n_e pedestal is shifted out by $r/a = 0.01$. EPED1 does not take a shift into account, which may explain why the code overestimates the pedestal temperature for the lowest ρ^* DIII-D point in this study (Figure 7a). The large variation in ELM size in the DIII-D ρ^* scan remains unexplained. The variation in the relative profile position leads only to a small variation of the peeling ballooning mode structure. Previous observations [5] indicating that the pedestal structure variation plays a role in the broadening or narrowing of the mode structure, thereby affecting the ELM size through a variation in ELM affected area, are not confirmed by the experiments in this study.

ACKNOWLEDGEMENTS

This work was partly funded jointly by the UK Engineering and Physical Sciences Research Council and by the European Communities under the contract of Association between EURATOM and UKAEA. It was carried out within the framework of the European Fusion Development Agreement. The views and opinions expressed herein do not necessarily reflect those of the European Commission. This work was supported in part by the U.S. Department of Energy under Grant No. DE-FC02-04ER54698, DE-FG02-89ER53296.

REFERENCES

- [1]. M.N.A. Beurskens *et al*, Nuclear Fusion **48** (2008) 095004
- [2]. M.N.A. Beurskens *et al*, 22nd IAEA Fusion energy conference, Oct. 13-18, Geneva, (2008)

- [3]. J.W. Connor *et al*, Phys. Plasmas, **5**, 2687 (1998)
- [4]. J.R. Ferron, *et al*, 26th EPS Conf. on Plasma Phys. And Contr. Fusion, **23J**, 1201 (1999)
- [5]. M.E. Fenstermacher, T.H. Osborne *et al*, Nuclear Fusion **45** (2005) 1493–1502
- [6]. R.J. Groebnert *et al*, Plasma Phys. Control. Fusion **44** (2002) A265–A272
- [7]. Hatae T. *et al* Plasma Phys. Control. Fusion **40** 1073 (1998)
- [8]. A.E Hubbard *et al*, Plasma Phys. Control. Fusion **42** A15 (2000)
- [9]. G.T.A. Huysmans, Plasma Phys. Controlled Fusion **47**, B165 (2005).
- [10]. Kinsey J.E. *et al*, R.E. Phys. Plasmas **9** 1676 (2002)
- [11]. A. Kirk *et al*, Plasma Phys. Control. Fusion **46** (2004) A187–A194
- [12]. LL Lao *et al*. 29th EPS Conf. on Plasma Phys. and Contr. Fusion, 17-21 June 2002, Montreux
- [13]. A.W. Leonard *et al*, Journal of Physics: Conference Series **123** (2008) 012001
- [14]. A. Loarte *et al*, Plasma Phys. Control. Fusion **44** (2002) 1815-1844
- [15]. A. Loarte *et al*, Plasma Phys. Control. Fusion **45** (2003) 1549–1569
- [16]. A. Loarte *et al*, Physics of plasmas 11-5 (2004), 2668-2678
- [17]. G. Maddisson, 35th EPS Conference on Plasma Phys. and Contr. Fusion 9-13 June 2008, Greece
- [18]. M.A. Mahdavi *et al*, Nucl. Fusion **42** (2002) 52–58
- [19]. Martin Y. and ITPA threshold database working group, J. of Phys.: Conf. Ser. 123 (2008) 12033.
- [20]. D.A. Mossessian, *et al*, Physics of plasmas V10, number **3**, (2003) 689-698
- [21]. I. Nunes *et al*, Nuclear Fusion **44** (2004) 883–891
- [22]. I. Nunes *et al*, Nuclear Fusion **45** (2005) 1550-1556
- [23]. T. Onjun *et al*, Physics of plasmas V9, number 12, (2002) 5018-5030
- [24]. T.H. Osborne *et al*, Plasma Phys. Control. Fusion **40** (1998) 845–850
- [25]. T.H. Osborne *et al*, 19th IAEA Fusion Energy Conference, October 14–19, 2002, Lyon, France
- [26]. T.H. Osborne *et al*, 45th APS Div. of Pl. Phys Meeting, October 27-31, 2003, Albuquerque, US
- [27]. N. Oyama *et al*, Nuclear Fusion **45** (2005) 871–881
- [28]. N. Oyama *et al*, Plasma Phys. Control. Fusion **48** (2006) A171–A181
- [29]. Editors of ‘Progress in the ITER Physics Basis’, Nucl. Fusion **47** (2007) S1–S17
- [30]. R. Pasqualotto *et al*, 2004 Rev. Sci. Instrum. **75** 3891
- [31]. Porter G D, Moller J, Brown M, and Lasnier C 1998 Phys Plasmas **5** 1410
- [32]. F Ryter *et al*, Plasma Phys. Control. Fusion **43** (2001) A323–A338
- [33]. S. Saarelma, *et al*, Plasma Phys. Control. Fusion **51** (2009)
- [34]. G. Saibene *et al*, Nuclear Fusion, Vol. **39**, No. 9, 1999, 1133
- [35]. G. Saibene *et al*, Nucl. Fusion **45** (2005) 297
- [36]. G Saibene *et al*, Nucl. Fusion **47** (2007) 969–983
- [37]. G. Saibene *et al*, et al, 22nd IAEA Fusion energy conference, October 13-18, Geneva, (2008)
- [38]. R Scannell *et al*, Rev. Sci. Instrum. **77**, 10E510 (2006)

- [39]. P.B. Snyder, *et al*, Phys. Plasmas **9**, 2037 (2002)
 [40]. P.B. Snyder, *et al*, Nucl. Fusion **44**, 320 (2004).
 [41]. P.B. Snyder, *et al*, 22nd IAEA Fusion energy conference, October 13-18, Geneva, (2008)
 [42]. P.B. Snyder, *et al*, Phys. of Plasmas **16**, 056118 (2009)
 [43]. H. Urano *et al*, Nucl. Fusion **48** (2008)
 [44]. H.R. Wilson, *et al*, Phys. Plasmas, **9**, 1277 (2002).
 [45]. Zhitlukin *et al*, Journal of Nuclear Materials **363–365** (2007) 301–307

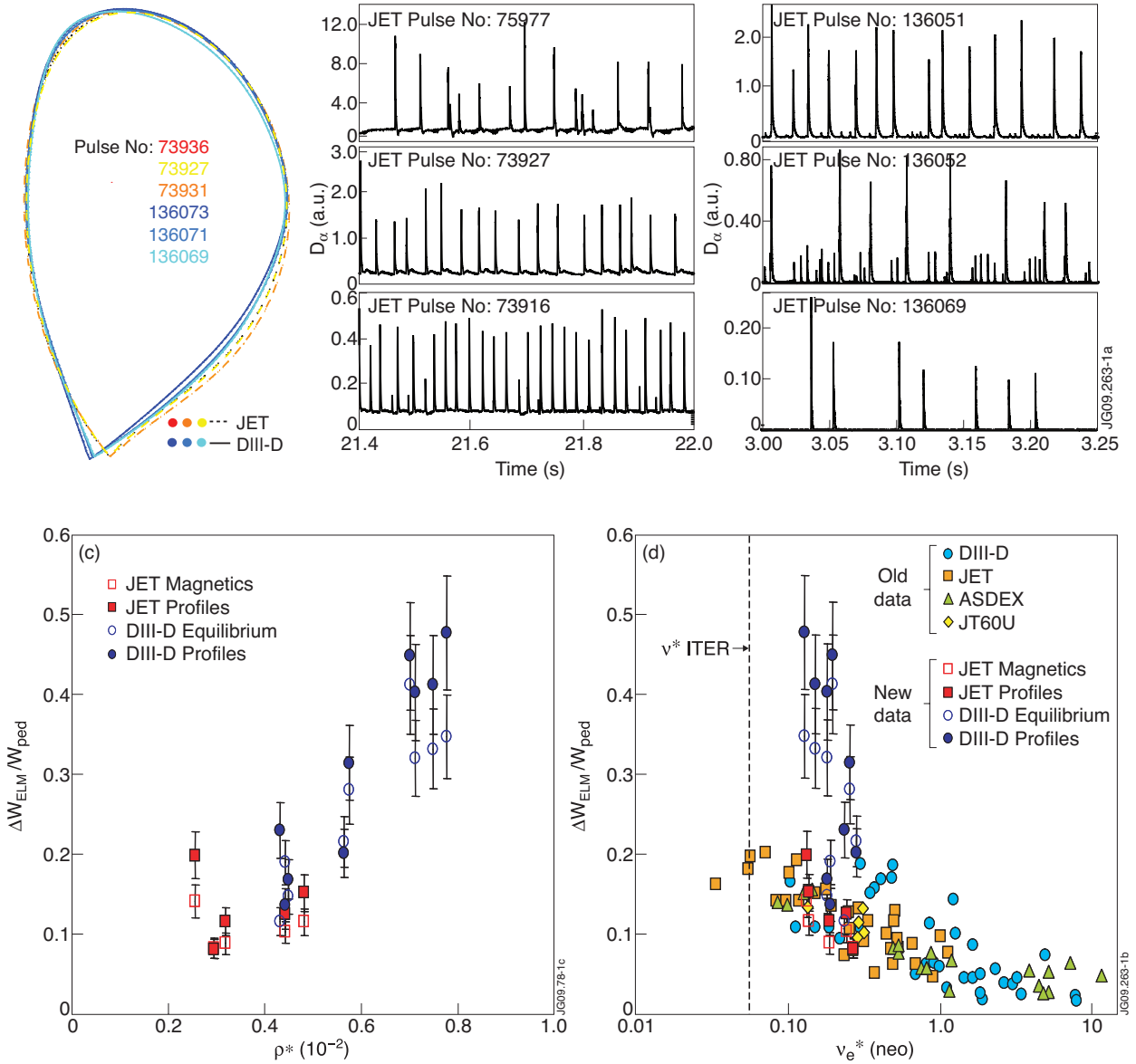


Figure 1: (a) Plasma configuration shape match at JET and DIII-D b) Divertor $D\alpha$ emission for JET and DIII-D c) ELM energy losses normalised to the pedestal energy as a function of ρ^* . Two methods were applied in establishing the ELM size, which give consistent results: determined from profiles changes (closed symbols) and determined from equilibrium reconstruction (DIII-D) or diamagnetic loop measurements (JET) (open symbols) d) ELM energy losses compared to data of the multi-device comparison study [15] as a function of ν_e^* .

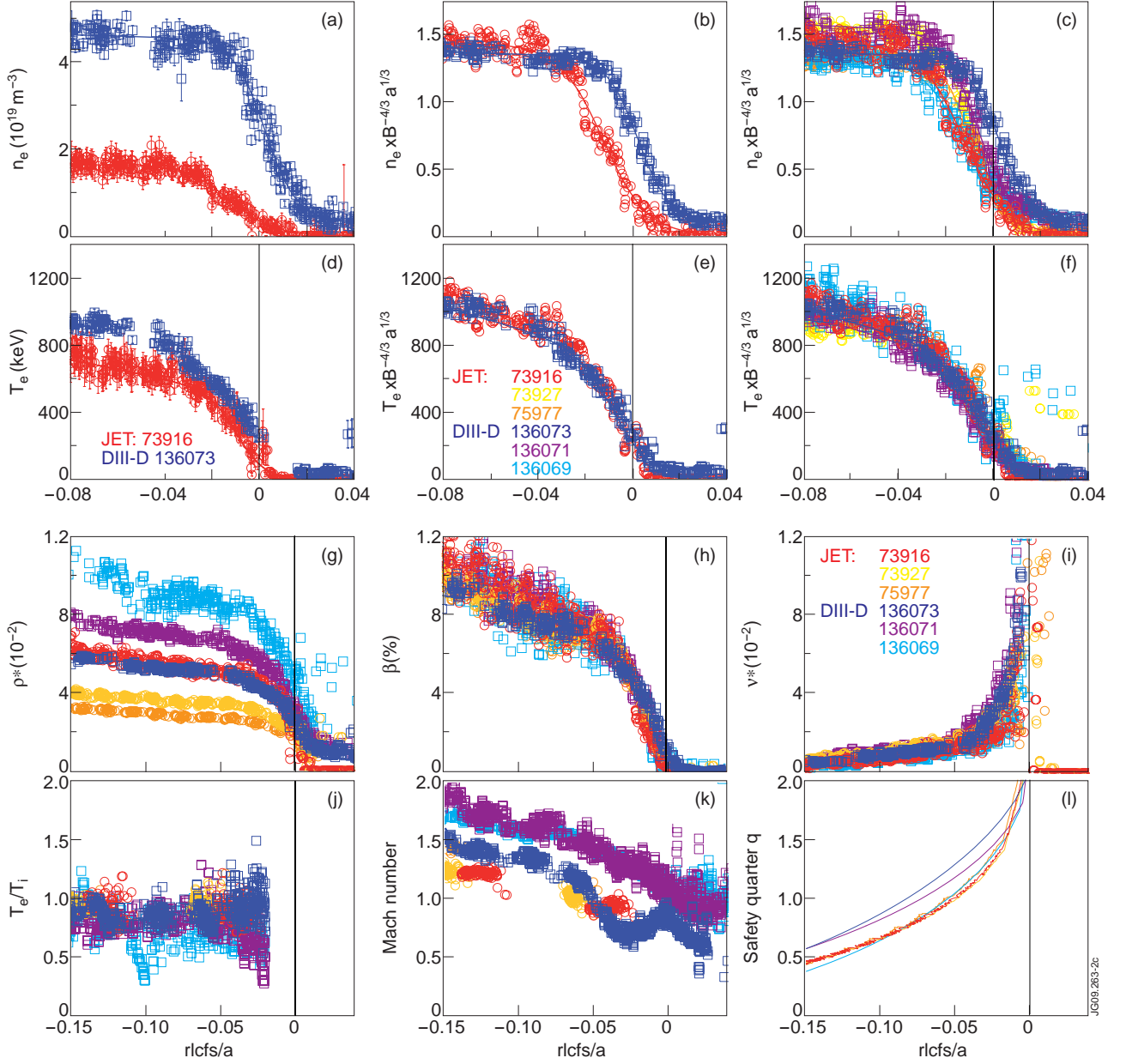


Figure 2: T_e and n_e profiles and dimensionless parameters for the low triangularity ρ^* scan. a,d) T_e and n_e profiles for the identity match. b,e) scaled T_e and n_e profiles for the identity match c,f) scaled T_e and n_e profiles for the ρ^* similarity scan. g-l) profiles of ρ^* (using T_e), β_e , v_e^* , T_e/T_i , Mach number (D2 mass/C velocity) and q -profile. For clarity a smoothing of 5 spatial data points has been applied.

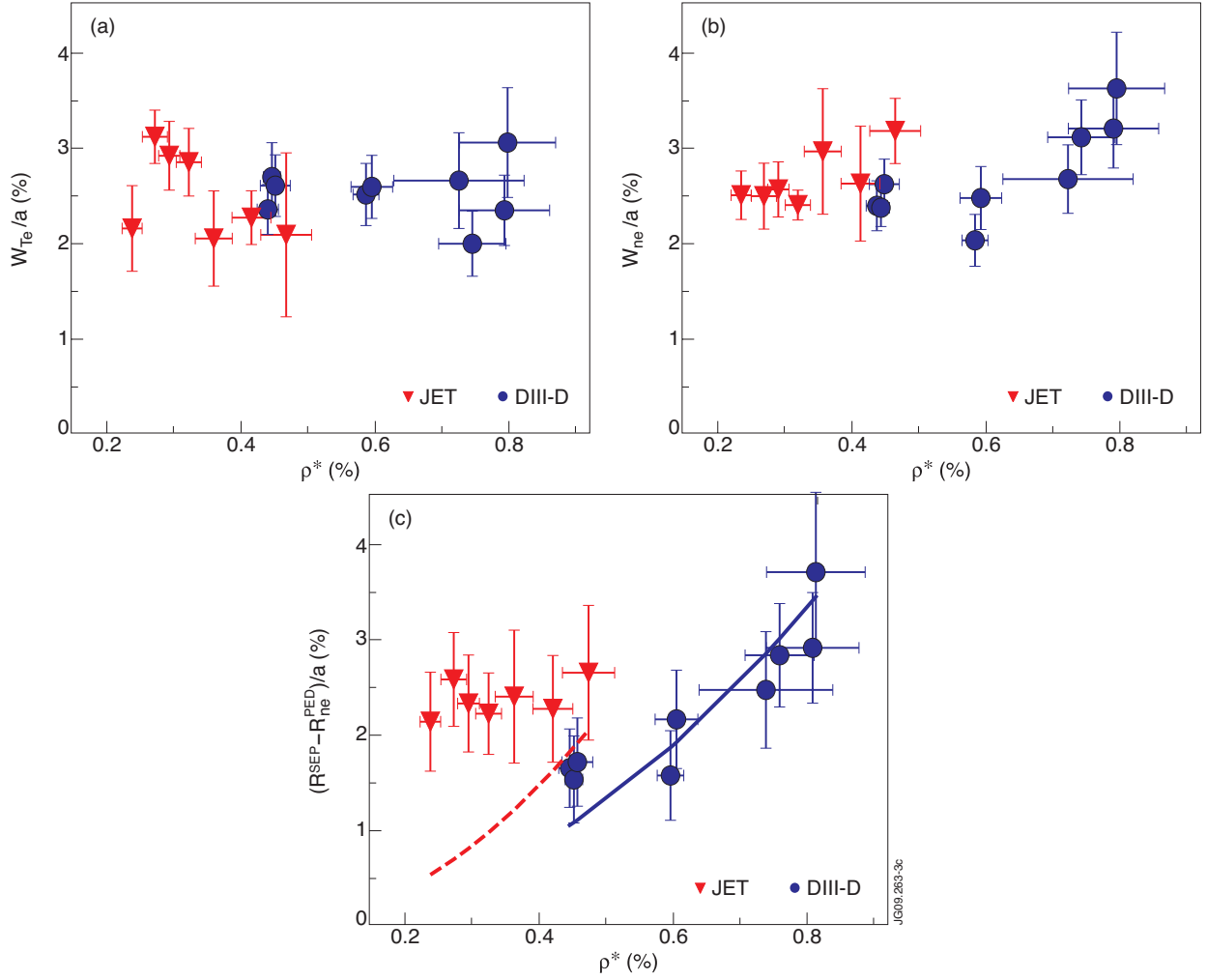


Figure 3: Pedestal analysis using $mtanh$ fitting functions and deconvolution technique. The parameters are given in the midplane normalised to the minor radius a) T_e pedestal width versus ρ^* , b) n_e pedestal width versus ρ^* , c) n_e width inside separatrix versus ρ^* for comparison with the neutral penetration model: position of the top of the n_e pedestal relative to the separatrix. Blue solid line: fit of the DIII-D data to ρ^{*2} scaling expected for neutral penetration. Red dashed line: scaling of the ρ^{*2} DIII-D line to the JET data.

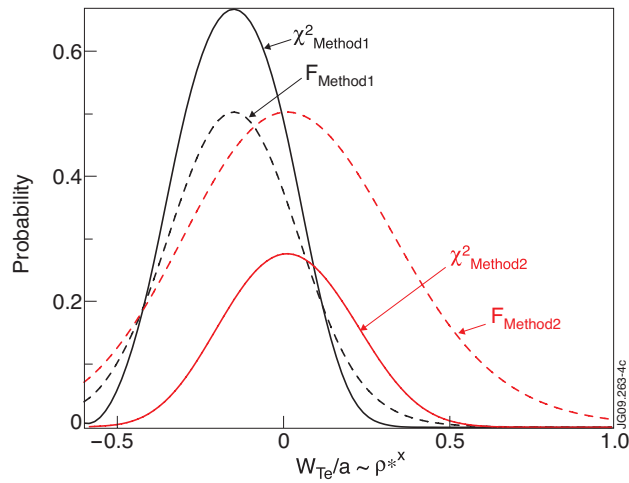


Figure 4: χ^2 probability and F test probability of ρ^* scaling exponent in W_{Te} fit for two methods of error handling (see text).

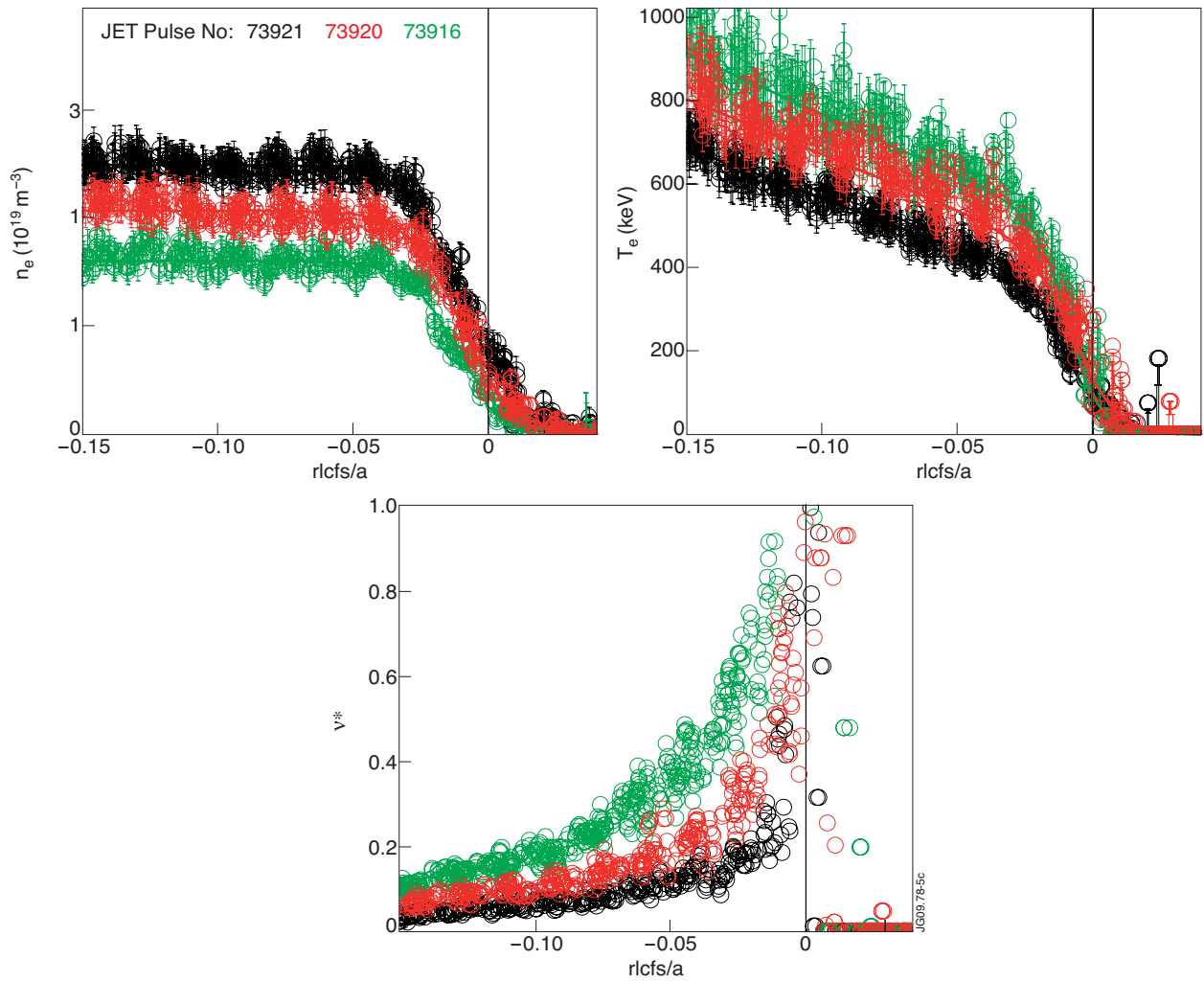


Figure 5: Collisionality scan on JET. ($\delta_{av} = 0.28$, $I_p = 1\text{MA}$ and $B_T = 1.1\text{T}$, $P_{NBI} = 4.5\text{MW}$)

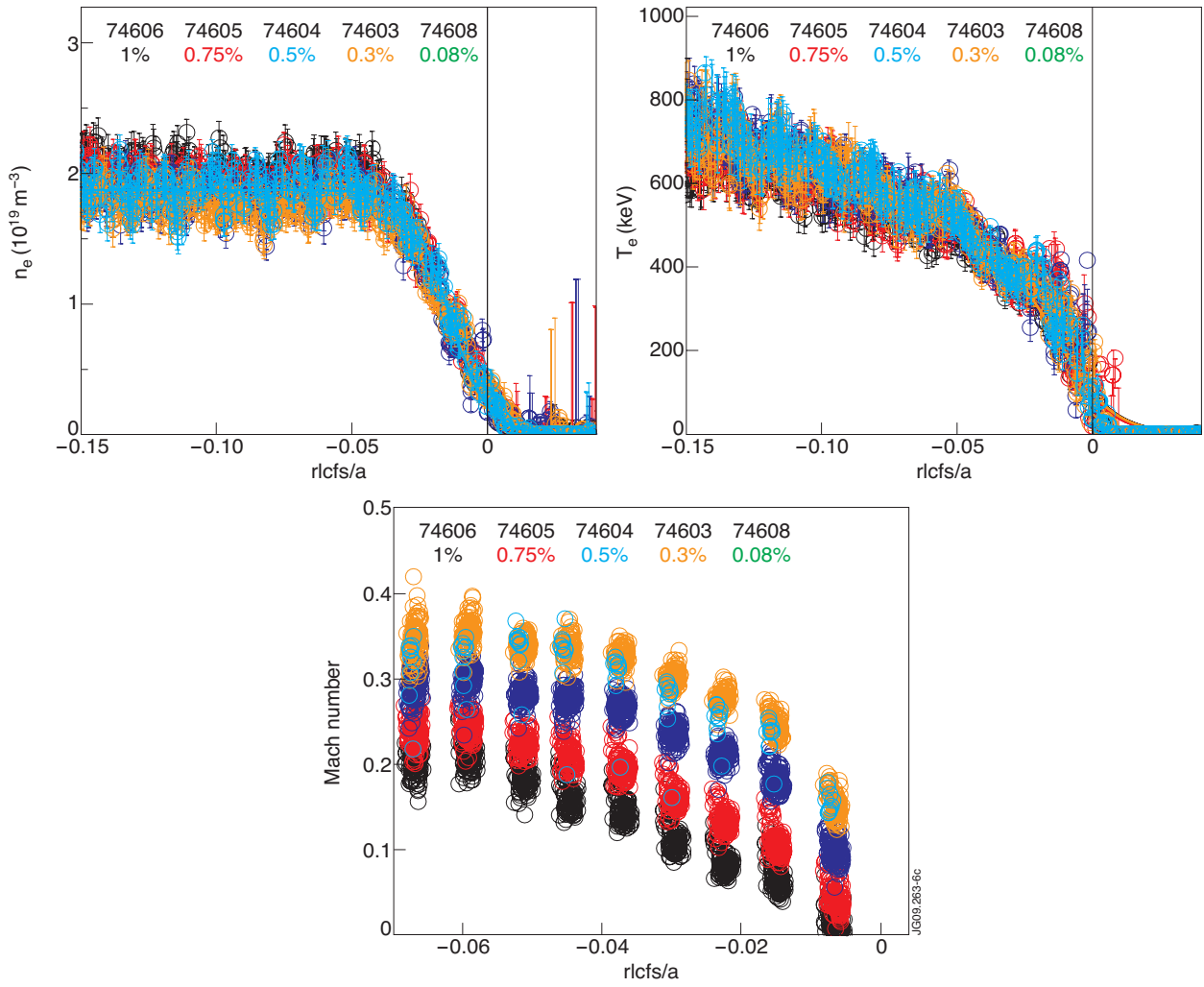


Figure 6: Ripple scan on JET respectively at 0.08, 0.25, 0.5, 0.75 and 1% ripple.
 ($\delta_{av} = 0.28$, $I_p = 1 \text{ MA}$ and $B_T = 1.1 \text{ T}$, $P_{NBI} = 4.5 \text{ MW}$)

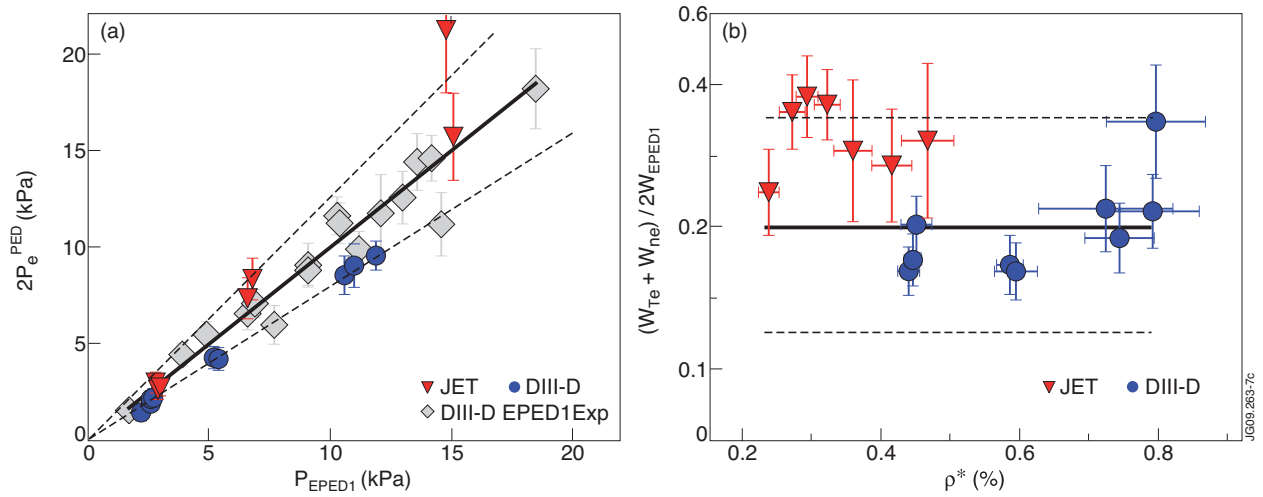


Figure 7: Comparison of pedestal data from the ρ^* scaling experiment with the EPED1 model. The dotted lines represent the range of variability in the model predictions (see text). a) Measured versus predicted pressure at the pedestal top; gray symbols are other DIII-D data covering a wide range of shapes and β 's. b) Ratio of measured and predicted pedestal width versus ρ^*

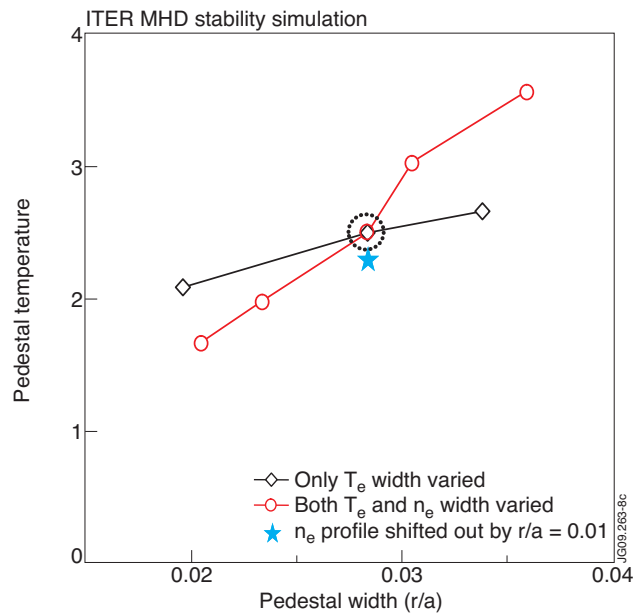


Figure 8: ITER MHD stability simulation. The dashed circle indicates the T_e prediction using the reference profiles from JET Pulse No: 75977.